

Numerical investigation of a narrowband absorber with a simple structure

AKANKSHA NINAWA,¹ ANUJ DHAWAN,^{1,3}  AND XIANFAN XU^{2,4} 

¹Department of Electrical Engineering, Indian Institute Technology Delhi, Hauz Khas, New Delhi 110016, India

²School of Mechanical Engineering and Birck Nanotechnology Center, Purdue University, West Lafayette, Indiana 47907, USA

³adhawan@ee.iitd.ac.in

⁴xxu@purdue.edu

Abstract: We propose a simple structure of a metamaterial (MM) to achieve near-perfect narrowband absorption. This MM utilizes both a plasmonic antenna and its complimentary structure for trapping electromagnetic fields, without the use of a complete ground plate compared to conventional designs. The simple design opens a new possibility of engineering perfect absorbers that can be easily fabricated, and thus many potential applications in mid-infrared include thermal imaging, energy harvesting, localized biological sensing, optical tweezers, and laser beam shaping.

© 2020 Optical Society of America under the terms of the [OSA Open Access Publishing Agreement](#)

1. Introduction

Plasmonic nanostructures and MMs have attracted significant attention in research due to their unique optical properties such as negative refractive index [1], super-lenses [2], and plasmonic reflectors and absorbers [3]. Narrowband absorbers based on intricate designs of plasmonic MMs have been investigated due to their potential applications in thermal emitters [4], sensitive localized refractive index detection [5], and sensing [6]. Typical plasmonic absorbers are based on the conventional tri-layered metal-insulator-metal (MIM) array designs, which essentially incorporate a dielectric spacer layer sandwiched between a base metal ground plate and a top metal nanostructured film [7–19]. The ground plate in conventional designs blocks transmission completely, resulting in a background reflection which is suppressed due to its destructive interference with resonances in top metal nanostructured film and thus the energy is largely absorbed [20].

Diabolo nanoantenna is an intriguing geometry which is capable of strongly confining and enhancing magnetic field. The principle phenomenon of funneling of the high current density into the metallic bridge resulting in magnetic field confinement and enhancement has been explained in [21]. Plasmonic diabolo multi-bowtie antenna with Fano resonance and its aperture counterpart for spectral sorting applications have also been studied [22]. In this letter, we propose an enhanced absorption MM which distinguishes from the conventional MIM designs of narrowband absorbers as it does not require a complete metal ground plate for the desired functionality. The absorber is based on a simple design which can be fabricated in two steps: a lithography step, which can be electron beam lithography, optical lithography, nanoimprint lithography, or laser direct write, and a metallization step. Figure 1 shows the schematic of the proposed MM which is essentially a periodic array of a lattice unit comprising of a combination of a bowtie aperture antenna (BAA) [23] at the bottom and an upper nanostructured diabolo antenna (DA), separated by an intermediate relatively thick dielectric spacer. The two meta-surfaces are ‘Babinet’ counterparts which can be understood as providing the resonant states of MM with complementary electric and magnetic field responses based on Babinet’s reciprocity principle. The structures can be fabricated by a simple two-step fabrication process: bowtie array lithography

on glass substrate followed by metallization of gold. The lithography step can be carried out using, for example, two photon polymerization (TPP) laser- direct-write technique [24]. The two-step fabrication is illustrated in Fig. 1(d). The optimized structural dimensions are obtained by the geometric variation of parameters to achieve vanishing reflection and transmission, corresponding to maximum absorption. In this paper, we study the geometry and physical mechanism by which our MM achieves near perfect absorption. The corresponding electric and magnetic field enhancements are achieved by the localized surface plasmon resonance (LSPR), the lightning rod effect, trapping of electromagnetic (EM) fields, and Fano resonance. We further analyze the absorption spectra (A-spectra) and study the existence of Fano resonance and discuss the typical Fano-resonant line-shapes noted in the near-field spectral responses correlated with far-field A-spectra.

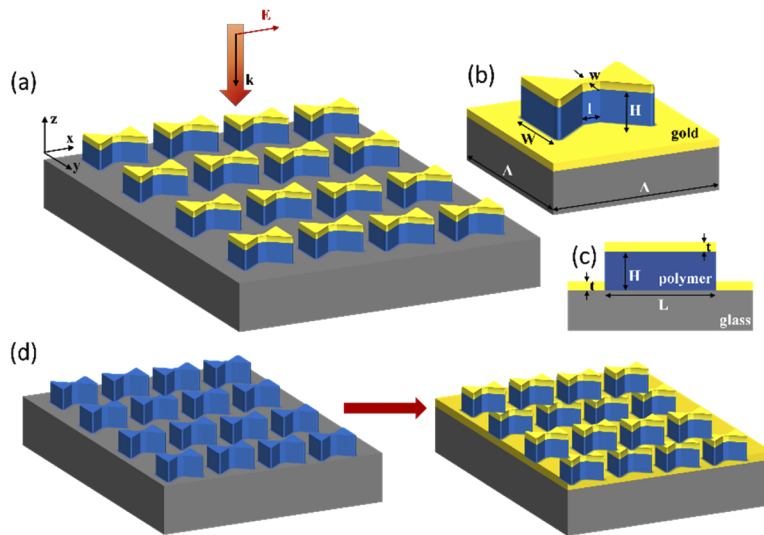


Fig. 1. (a) Schematic of gold coated diablo array antenna based under x-polarized electric field illumination. (b) Lattice single unit of the array with structural parameters indicated. (c) Vertical cross-section view of the lattice single unit cell showing the meta-surface layer by layer design. Optimized dimensions are lattice periodicity, $\Lambda = 4 \mu\text{m}$; thickness of dielectric deposited on glass, $H = 600 \text{ nm}$; antenna length, $L = 2.5 \mu\text{m}$; antenna width, $W = 1.5 \mu\text{m}$; neck length of antenna, $l = 600 \text{ nm}$; neck width of antenna, $w = 250 \text{ nm}$, thickness of gold coating, $t = 55 \text{ nm}$. (d) Schematic of the two-step fabrication process, a lithography or laser-direct-write process followed by a metallization process.

2. Results and discussion

The numerical investigation of the proposed absorber is done by employing the frequency domain finite-element method [25]. The optical properties of gold are taken from [26]. The relative permittivity of the dielectric layer employed in the present numerical study is 2.25, which is the typical value of photo-polymer that can be patterned using lithography or laser direct write. Figure 2(a) shows reflectivity R , transmissivity T , and absorption A spectra of the optimized antenna under TE wave illumination (incident electric field vector \mathbf{E} lies along the length of diablo antenna) with wave vector \mathbf{k} of incident illumination normal to the meta-surface. From the spectra, we note that our MM shows an absorption of 95% at $4.065 \mu\text{m}$. The enhanced electromagnetic fields due to localized surface plasmon resonance and lightning rod effect, and the enhanced current in the top layer due to these effects contribute towards the enhanced

absorption in the proposed MM. A detailed analysis of the geometric parameters presented later in the text shows the effect of resonance on absorption. The Fano resonance of the MM also results in enhanced absorption. Further, the absorption maxima, vanishing reflection dip, and the residual transmission minima all occur at $4.065 \mu\text{m}$. Another resonant state is noted at $4.277 \mu\text{m}$. The perspective views of spatial distributions of E- and H- fields at the resonances are shown in Fig. 2(b). We choose a set of locations on the structure corresponding to electric and magnetic field hotspots (Fig. 2(c)) seen from the perspective views which are labelled as $E1 \dots E4$ for E-field hotspots and $H1 \dots H3$ for H-field hotspots. From E-field spectral responses (Fig. 2(d)) at the locations, it is found that at $E4$, the electric field at $4.065 \mu\text{m}$ is $\sim 3.8 \times 10^8 \text{ V/m}$ as compared with the incident field of $\sim 7 \times 10^6 \text{ V/m}$. Hence, the electric field enhancement at point $E4$ at $4.065 \mu\text{m}$ is ~ 54 . The H-field spectral responses for the hotspots are shown in Fig. 2(e). We also note a Fano resonance asymmetric spectral line-shape specific to H-field spectral response at $H3$ with large amplitudes of the order $\sim 5.7 \times 10^5 \text{ A/m}$ and $\sim 6.5 \times 10^5 \text{ A/m}$ at the corresponding Fano resonance peaks respectively, compared with the incident field of $\sim 1.8 \times 10^4 \text{ A/m}$. Hence, the magnetic field enhancement at point $H3$ at $4.277 \mu\text{m}$ is ~ 35 . A detailed discussion of this Fano-resonance and its correlation with far-field A-spectra is presented later in the text. Results for TM wave illumination are given in Appendix A. The far-field R, T and A spectra for the antenna is given in Appendix A: Fig. 6(a) and the E- and H-field surface distributions at surfaces $S1$ and $S2$ are given in Appendix A: Fig. 6(b).

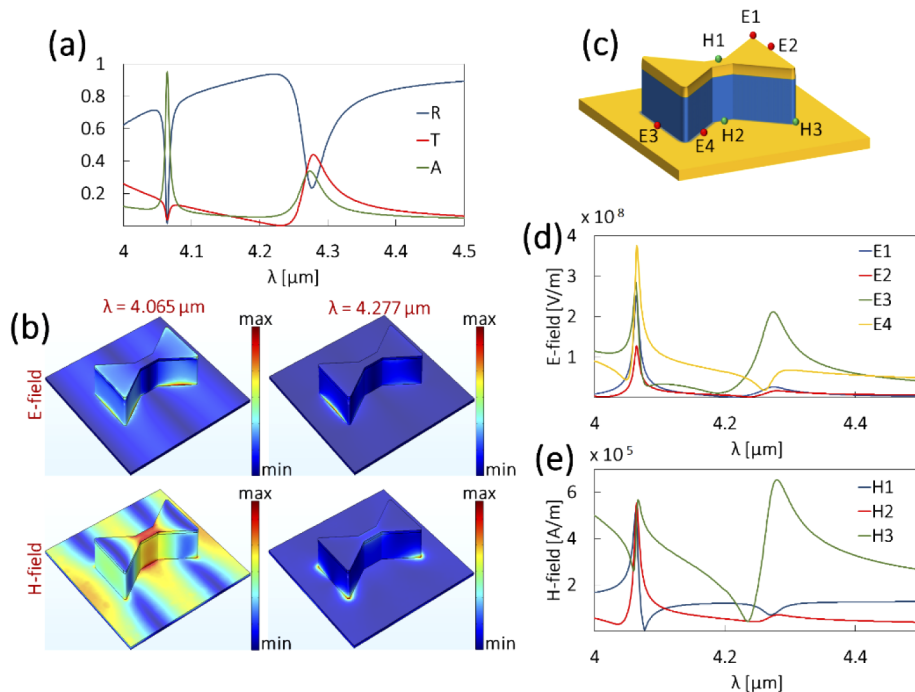


Fig. 2. FEM calculations (a) R, T, A of our MM for x-polarized incident light with resonances at $4.065 \mu\text{m}$ and $4.277 \mu\text{m}$. (b) Perspective views of E-field and H-field spatial distributions at resonances (c) Locations of E- and H-field hotspots (d) Spectral near-field electric field intensities at E-field hotspots (e) Spectral near-field magnetic field intensities at H-field hotspots.

To understand the significant confinement of EM fields, we analyze the plasmonic states at two resonances from the near-field distributions on DA and BAA on their transverse surfaces $S1$ (upper exposed DA) and $S2$ (bottom BAA) (Fig. 3). At $\lambda = 4.065 \mu\text{m}$, on $S1$, E-field is mainly

confined at the corners of the antenna. The DA as a nanoparticle dimer, polarizes the incident E-field along the corners of the metal triangles due to localized SPs at the air-metal interface, essentially forming an electric quadrupole (EQ) mode. Further, optimized antenna dimensions combined with the resonant LSPR and the lightning rod effect result in maximum local field enhancement. The H-field confinement in the conducting metal bridge connecting the two metal triangles in DA on S1 occurs as predicted for the proper optical excitation. The metal bridge acts as an inductor around which the H-field is azimuthally polarized. On S2, the BAA dimer confines E-field along the metal-dielectric (M-D) interfaces of the aperture triangles for the incident optical excitation. In literature, such confinement of optical energy has been referred to as a hybrid hexapolar-quadrupolar (EHQ) mode [27]. The H-field is mainly confined at the interfaces of the M-D bridge and at the ends of antenna corners. At $\lambda = 4.277 \mu\text{m}$, E-field confinement on S1 is somewhat dipolar, the field confinement is however not as strong as noted for $\lambda = 4.065 \mu\text{m}$. The corresponding H-field is mainly along the parallel edges of the conducting metal bridge because of the relatively weak electric funneling from the triangular metal sections. On S2, due to the localized SPs at the M-D interface, the BAA dimer strongly confines the E-field along the vertical edges of the metal triangles forming an electric dipole (ED) mode, while the H-field confinement resembles a magnetic quadrupole (MQ) mode. We will also discuss the effect of these modes later in the text in the context of Fano resonance. The enhanced EM fields lead to enhanced absorption. Further, it should be mentioned that the substantially large intensities of EM fields can also be understood by the optical trapping of EM energy in the dielectric spacer between the nanoantenna and nanocavity meta-surfaces for an optimized spacer thickness. This leads to our discussion on the influence of the variation of structural parameters on the functionality of our proposed MM as an absorber by which we also substantiate our choice of the optimized dimensions.

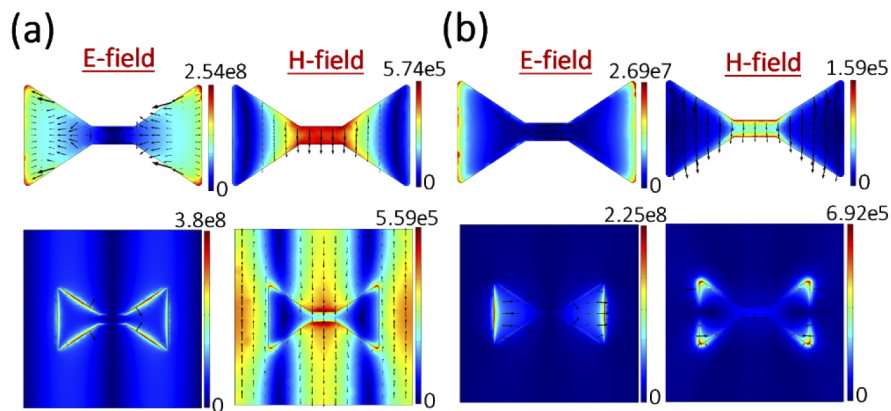


Fig. 3. E-field [V/m] and H-field [A/m] distribution plots and field directions at resonance wavelengths (a) $4.065 \mu\text{m}$ and (b) $4.277 \mu\text{m}$ along the transverse XY plane on surfaces S1 (row 1) and S2 (row 2).

We study the influence of variation of structural parameters, namely, H , L , W , Λ , l , w and t of the antenna, under TE wave illumination and have found that, H , L , W and Λ have the largest effects on absorption. First, the absorber is significantly affected by the variation of L (Fig. 4(a)). It is found that as L is varied from the optimized case ($2.5 \mu\text{m}$), with other parameters as $\Lambda = 4 \mu\text{m}$, $H = 600 \text{ nm}$, $W = 1.5 \mu\text{m}$, $l = 600 \text{ nm}$, $w = 250 \text{ nm}$, $t = 55 \text{ nm}$, the absorption peak at $4.065 \mu\text{m}$ sharply reduces from 95% to 30% for $L = 3 \mu\text{m}$ at $4.153 \mu\text{m}$. We note two plasmonic states from A-spectra for L variation. For the subsequent discussion, we refer to these first band and second band plasmonic states as M1 and M2, respectively. For M1, from the E-field surface

distribution at S1 (Appendix B: Fig. 7(c)), the strength of the LSPR EQ mode is most pronounced for optimized L and decreases for subsequent cases. It is found that this occurs in the background of a spectrally broad transmission at M1 (Appendix B: Fig. 7(b)), where the energy is ‘leaked’ though the MM. The strength of LSP EQ mode for smaller L confines the energy to not be ‘leaked’ in the form of transmission. For small values of L , the oscillation of conducting electrons dominantly converts the re-radiated energy of LSP EQ mode into strong far-field absorption. The red-shifted spectra with increasing L at M1 are due to the reducing restoring force as the antenna spans a larger length. Next, with increase in L , the energy of plasmonic mode at M1 starts splitting into M2 with the L variation spectra blue-shifted with increase in L . The blue-shift at M2 can be attributed to the coupling effects in far-field which take precedence over the coupling effects in near-field when the antenna size becomes much smaller in comparison to the resonant wavelength of interacting light at M2 [28]. The coupling effects in far-field occur because of scattered far-fields (Appendix B: Fig. 7(a)) characterized by dipolar near-field distributions which is indeed noted on S1 for L variation at M2 LSP wavelengths corresponding to each varied L . The dipolar strength increases with increase in L . Optimization of L is with respect to the first absorption band. We did not study the effect of reducing L further as we chose reasonably large sizes for easy fabrication.

The width of the antenna also has a significant effect on the performance of our absorber. The A-spectra for different W (with other parameters as $\Lambda = 4 \mu\text{m}$, $H = 600 \text{ nm}$, $L = 2.5 \mu\text{m}$, $l = 600 \text{ nm}$, $w = 250 \text{ nm}$, $t = 55 \text{ nm}$) in Fig. 4(b) reveal that as W increases, the resonant peak substantially reduces and is redshifted. The spatial field distributions on S1 (not shown here) confirm a rather prominent EQ mode and a stronger confinement of H-field in the metal bridge for smaller W . $W = 1.5 \mu\text{m}$ is optimum for the proposed absorber illuminated under TE polarization.

We next study the influence of variation of H on our MM absorber. From A-spectra (Fig. 4(c)), it is noted that with increase in H , absorption increases, and $H = 600 \text{ nm}$ is optimum. The other parameters are $\Lambda = 4 \mu\text{m}$, $L = 2.5 \mu\text{m}$, $W = 1.5 \mu\text{m}$, $l = 600 \text{ nm}$, $w = 250 \text{ nm}$, $t = 55 \text{ nm}$. The relatively thick spacer in our hybrid bi-layer meta-surface reduces the possibility of interlayer coupling or ‘cross-talk’ between the independently generated plasmon resonances in the complementary nanoantenna and nanocavity ‘Babinet’ films. The enhanced absorption in our MM arises from the destructive interference between scattering from the two resonator films and their independently generated resonances leading to cancellation of total background reflected energy and thus the light is efficiently manipulated to result in a dominant absorption response from the MM. The far-field reflection spectra for H variation (not shown here) confirm near vanishing reflection for $H = 500 \text{ nm}$ and above, while for thinner films, in particular for $H < 300 \text{ nm}$, the total reflection is quite significant. Further, the near-field distributions along the longitudinal ZX plane (Appendix B: Fig. 8) shows intense light-matter interactions by the optical trapping of EM fields within the spacer with increase in H , indicating a longer path length travelled by light within the spacer thus resulting in enhanced absorption. We further note that the far-field A-spectra are redshifted with increase in H . This response can be analytically understood from the decoupled interference model for normal incidence proposed in [29–31], wherein a typical cross-resonator array MM absorber with a complete ground plane is used based on interference theory. In that study, it is shown that the resonant frequency of near-perfect absorption of the MM occurs at a frequency lower than the resonant frequency of upper resonator (in our case, DA), while neglecting the presence of the ground plate to obtain reflection and transmission coefficients at the air-spacer interface with the cross-resonators. For each spacer thickness, a phase matching condition occurs between antenna mode and reflection mode, resulting in a resonant frequency of near perfect absorption for that spacer thickness. In our MM, the ground plate is not perfectly reflecting as it is an aperture film. However, we still approximate the phase of the reflected wave from the nanocavity film as π for normal incidence of wave in our complementary design of the two meta-surface films. The effective phase between antenna mode

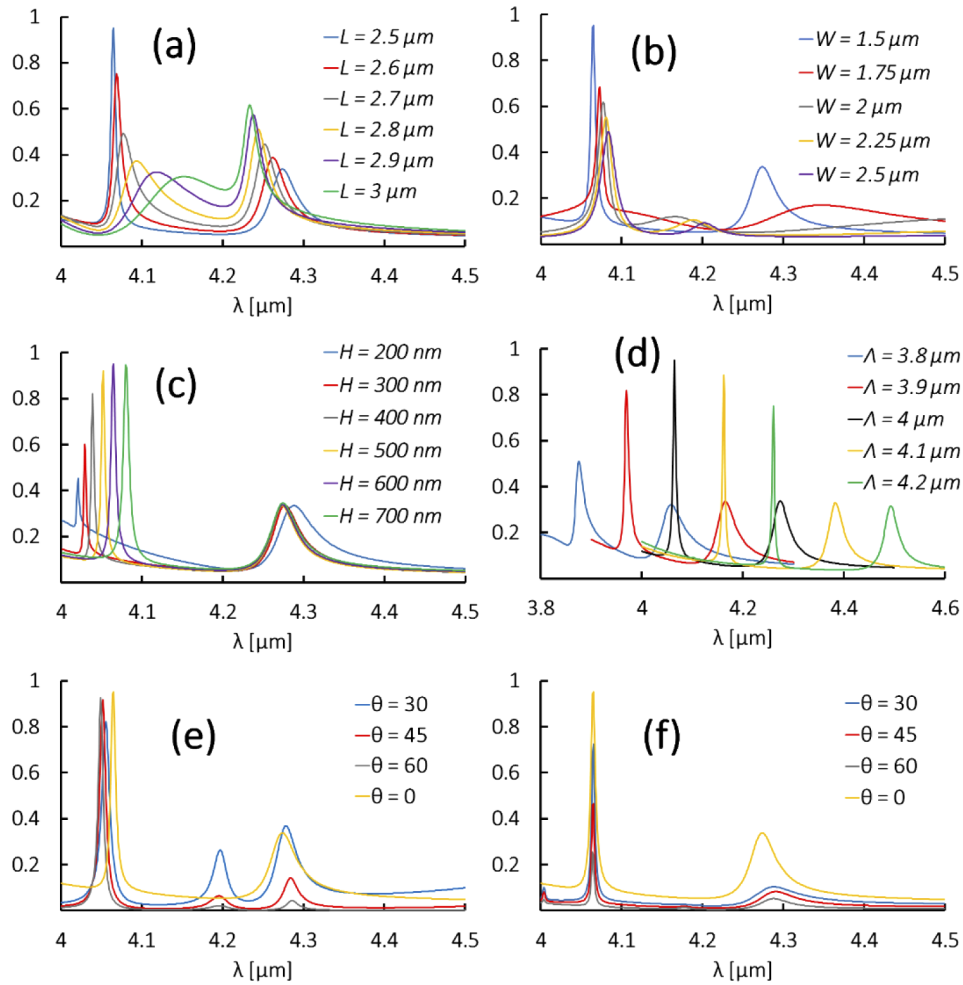


Fig. 4. Far-field A-spectra for variation of (a) L (b) W (c) H (d) Λ (e) θ in XZ plane and (f) θ in YZ plane.

and reflection mode is thus given by, $\varphi = 2\beta + \varphi_{21} + \pi, \sim 2\pi$. Here β is propagation phase and φ_{21} is reflection coefficient phase (after reflection from bottom BAA film) which will give positive values for frequencies lower than the resonant frequency of upper resonator. The perfect phase matching condition for an ‘optimized’ H for absorption maxima occurs when the reflection from the upper DA resonator destructively interferes with the multiple reflections within the spacer to result in complete cancellation of the overall reflection of the MM, in agreement with the perfect absorption physics. Further, a direct mathematical relationship of spacer thickness with φ_{21} and wave number (k) [32], given by $H \approx \frac{\varphi_{21}}{2n_r k}$, where n_r is the real part of index of the spacer, for the lowest absorption frequency band, indicates that for increase in H , the resonant frequency of the MM redshifts with increase in φ_{21} and decrease in k as the peak absorption occurs below the resonant frequency of upper resonator.

We also studied the influence of variation of lattice periodicity Λ (Fig. 4(d)) and have found that the spectra redshifts with increase in Λ . The other parameters are $L = 2.5 \mu\text{m}$, $H = 600 \text{ nm}$, $W = 1.5 \mu\text{m}$, $l = 600 \text{ nm}$, $w = 250 \text{ nm}$, $t = 55 \text{ nm}$. For 2D array of plasmonic structure, the

wavelength at which SPP couples to the film changes according to [33,34]:

$$\lambda = \frac{\Lambda}{\sqrt{m^2 + n^2}} \sqrt{\frac{\epsilon_d \epsilon_m}{\epsilon_d + \epsilon_m}} \quad (1)$$

where Λ is the periodicity, m and n are integers, and ϵ_m and ϵ_d are the relative permittivities of metal and dielectric respectively. The permittivities do not change much in the wavelength range from 3.8–4.6 μm . Therefore, as the periodicity increases the SPP couples at a longer wavelength and a redshift is noted. Absorption for wavelength other than 4 μm decreases since the structure is optimized for 4 μm . Further, we studied the effect of variation of angle of incidence θ along the XZ and YZ planes shown in Fig. 4(e) and 4(f), respectively and found that the peak value of absorption is above 80% for θ greater than 60° in the XZ plane while absorption is highly sensitive to θ variation in the YZ plane with the peak absorption of 72% for $\theta = 30^\circ$ and 25% for $\theta = 60^\circ$. The decrease in absorption at inclined angles is due to the fact the structure is not completely covered by metal film when viewed from an angle. This indicates that the structure is best suitable for applications near normal incidence. We further analyzed the influence of fabrication imperfection when the walls of the dielectric layer would be covered with thin metal film of 20 nm and found that the absorption spectrum becomes broader around the peak absorption wavelength which is significantly redshifted compared with the ideal case in which the dielectric walls are not covered with metal. Further, the peak absorption reduces to $\sim 70\%$ for the non-ideal case as compared with the peak absorption of 95% for the ideal case. Hence, it is important to ensure that the side walls are not covered by metal film during the metallization process.

It is interesting to note that apart from substantially large EM near-field intensities, the spectral responses at EM field hotspots also exhibit the characteristic asymmetric Fano resonance like line-shapes around the absorption peaks (Fig. 5(c)). We thus investigate the nature of Fano resonances from the near-field spectral line-shapes as a comparative analysis of two geometrical cases: A and B, corresponding to strong and weak far-field A-spectra (Fig. 5(a)). We refer to the optimized geometry as Case A, with the parameters specified in Fig. 1. Figure 5(b) shows near-field distributions of E- and H-fields on surfaces S1 and S2 at resonances for case B. The geometrical parameters of case B are $\Lambda = 4 \mu\text{m}$; $H = 400 \text{ nm}$; $L = 2.9 \mu\text{m}$; $W = 2 \mu\text{m}$; $l = 600 \text{ nm}$; $w = 250 \text{ nm}$; $t = 55 \text{ nm}$.

In optimized case A, a Lorentzian symmetric resonance at 4.065 μm is noted from the spectral E-field at $E1$ (Fig. 5(c)). However, the line-shape of spectral E-field at $E2$, $E3$ and $E4$ resembles a typical asymmetric Fano line-shapes, suggesting the existence of Fano resonance. The anti-symmetric dark sub-radiant mode essentially determines the actual spectral resonance wavelength and is thus critical for the formation of Fano resonances. Further, a direct correlation between far-field A-spectrum and near-field intensities of Fano resonant nanostructures [35,36] indicates that a large near-field enhancement should occur around the Fano resonant spectral window. Naturally, Fano resonant nanostructures are bound to result in large EM near-field intensities which is realized by DA and BAA in our design. Further, from H-field spectral profiles, a reverse asymmetric Fano line-shape at 4.065 μm is noted at $H1$ which is also indicative of the Fano resonance. The asymmetric reverse Fano line-shape in H-field occurs due to the coupled plasmon mode at 4.065 μm resulted from the interference of a higher order plasmonic mode with a lower order dipole mode. The evidence of a clear Fano resonance at 4.065 μm is further validated from the non-Lorentzian asymmetric Fano line-shapes in H-field spectral profiles at $H2$ and $H3$. These asymmetric line-shapes could be attributed to the interference between EQ mode and MQ mode seen from the respective E- and H-field surface distribution plots on S2 at 4.065 μm . The spectral line-shape of H-field at $H1$ transforms from a narrowband asymmetric reverse Fano line-shape to an anti-resonant dip at 4.277 μm . This anti-resonant dip is seen to suppress the far-field absorption at the wavelength and, less confinement of H-field is seen in the bridge connecting the two triangles. The resonance at 4.277 μm resembles a quasi-Lorentz line-shape.

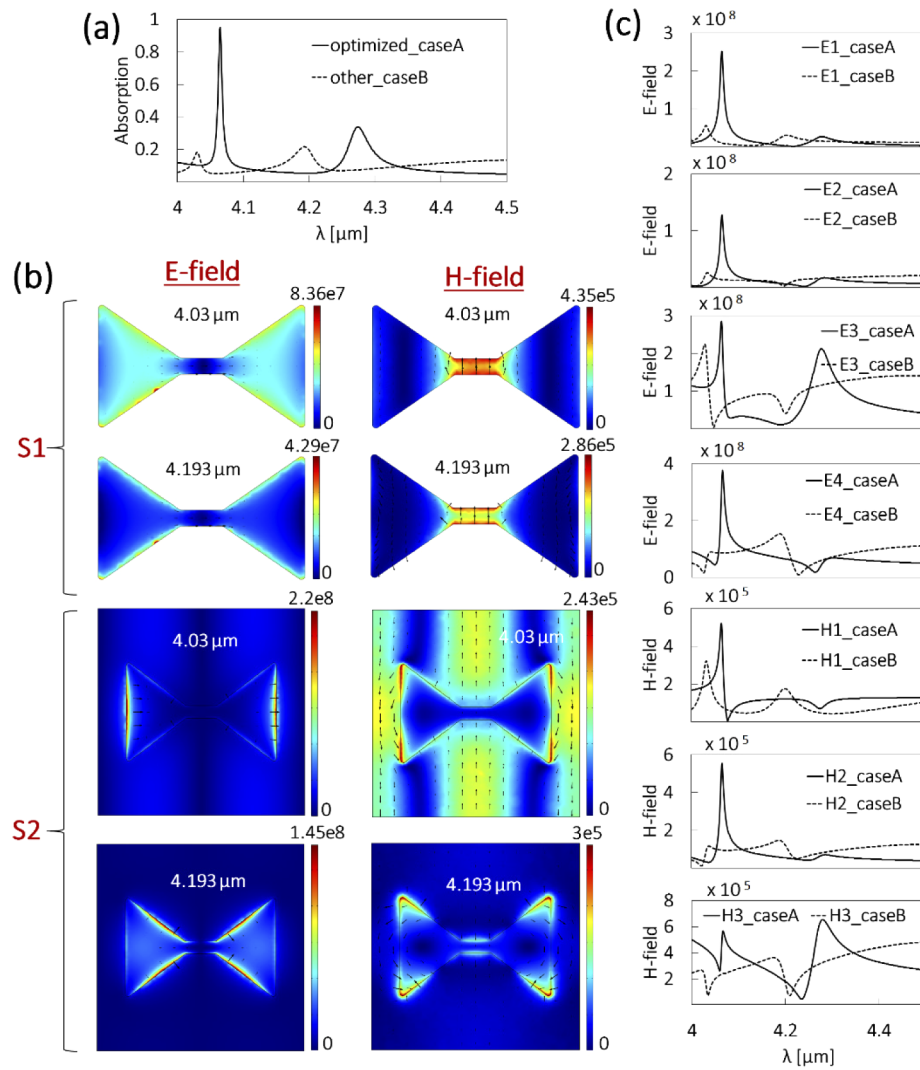


Fig. 5. Fano resonance investigation as a comparison of two geometrical cases of strong (optimized) and weak far-field absorptions. (a) Far-field A-spectra for cases A and B. (b) Near field spatial E-field and H-field at resonances on surface S1 (upper exposed diabolo antenna) and S2 (bottom bowtie aperture antenna) for Case B. (c) Spectral E- and H-field comparison of both cases at EM hotspots.

Another asymmetric Fano line-shape is noted at $4.277\ \mu\text{m}$ at $H3$ at which MQ mode is seen from the spatial H-field. The E-field direction at $4.277\ \mu\text{m}$ indicates that E-field emanates from left edge of the left triangle of DA, then diverges across the slanted edges of the left triangle. It then converges onto the right edge of DA and thus forms an effective ED mode. The E-field is thus seen as diverging on one side and converging on the other, indicating the presence of constructive and destructive interference modes around Fano resonance.

In weaker absorption case B, two Lorentz symmetric line-shapes corresponding to two resonances (at $4.03\ \mu\text{m}$ and $4.193\ \mu\text{m}$) in H-field spectral responses at $H1$ suggests the absence of Fano resonance. Further, at $E1$, similar Lorentzian symmetric E-field spectral line-shapes at the resonances also indicate the absence of any evidence of Fano resonance in the structure with weaker far-field absorption. However, a reverse asymmetric Fano line-shape is noted at $4.03\ \mu\text{m}$ in E-field spectral response at $E3$ which further transforms to an anti-resonant dip at $4.193\ \mu\text{m}$. This reverse asymmetric Fano line-shape can be explained by the interference between ED mode and MQ mode clearly seen from the respective surface E- and H- field distribution plots at $4.03\ \mu\text{m}$. Further, the line-shape of H-field at $H2$ transforms from an asymmetric non-Lorentzian Fano line-shape at $4.03\ \mu\text{m}$ to a reverse asymmetric Fano line-shape at $4.193\ \mu\text{m}$. It is also interesting to note that the line-shape of H-field at $H3$ exhibits two anti-resonant dips around the two resonances of the structure which may possibly indicate a suppressed Fano resonant behavior for the geometry.

3. Conclusions

In conclusion, we have proposed a simple design of an MM achieving near-perfect absorption (95%) without a complete ground plate. We have reported and discussed EM field enhancements, variation of structural parameters, and Fano resonance for enhanced absorption in our MM. The enhanced electromagnetic fields due to localized surface plasmon resonance and lightning rod effect contribute towards the enhanced current and hence absorption in the proposed MM. The designed MM can be realized in a simple two-step fabrication process, and hence can be easily implemented for various applications in IR.

Appendix A: FEM simulation results for TM wave illumination

Figure 6 shows R, T and A spectra of the antenna with optimized structural dimensions under TM wave illumination. The two plasmon resonances occur at $4.005\ \mu\text{m}$ and $4.262\ \mu\text{m}$ (reflection dips) at which we analyze the plasmonic states from the near-field distributions on DA and BAA on transverse surfaces S1 and S2 shown in Fig. 6(b). Upon comparison with surface near-field distributions for TE polarized illumination (Fig. 3), we note somewhat complementarily redistributed surface electric and magnetic field hotspots. The predicted swapping of electric and magnetic field hotspots observed on the meta-surface for TM polarization can well be explained by Babinet's principle of reciprocity between E- and H-fields. A point worth mentioning for TM polarization R/T/A spectra is that for the second plasmonic state, reflection dip ($4.262\ \mu\text{m}$), transmission peak ($4.254\ \mu\text{m}$) and absorption peak ($4.266\ \mu\text{m}$) do not coincide for either dip or peaks, as recently noted particularly for Fano resonant MMs [35,37,38].

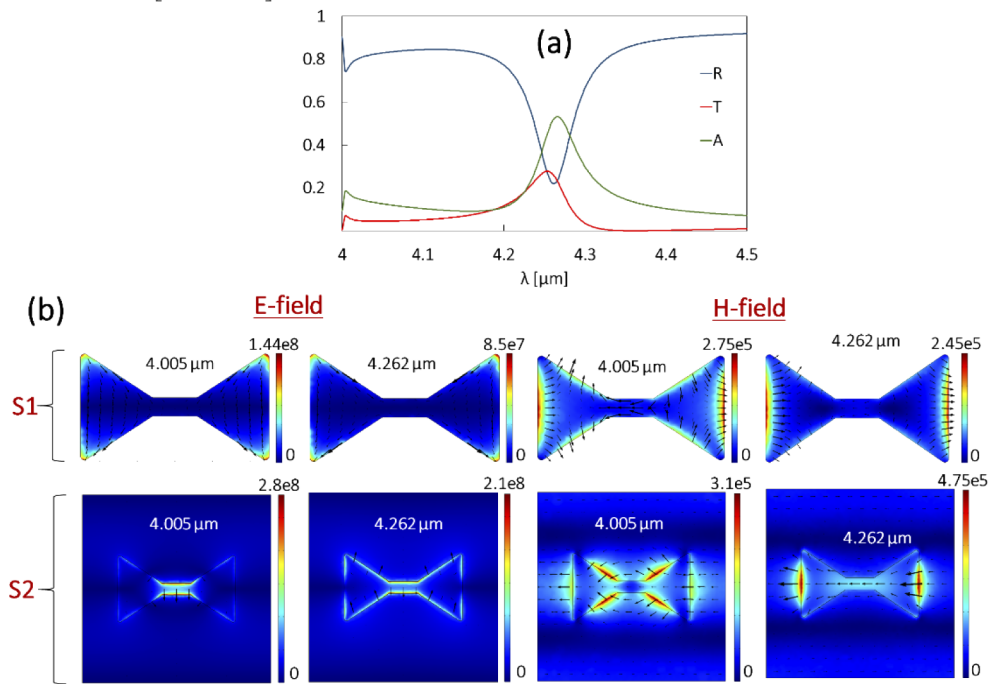


Fig. 6. FEM simulation results (a) R, T, A of our MM for TM polarized incident light with resonances at 4.005 μm and 4.262 μm . (b) Field distribution plots and field directions at resonances along the transverse XY plane on surface S1 [upper exposed diaboloid antenna] (row 1) and surface S2 [bottom bowtie aperture antenna] (row 2); E-field [V/m]: H-field [A/m]

Appendix B: FEM simulation results showing the effect of L variation on reflection and transmission and trapping of electromagnetic fields in dielectric spacer with H variation

The R and T spectra for variation of L is shown in Fig. 7(a-b). The decreasing strength of LSPR EQ mode at M1 (Fig. 7(c), column 1) with increase in L substantiates our choice of optimized L . Further, for M2, the dipolar near-field distributions (Fig. 7(c), column 2) which become prominent with increase in L indicate that the coupling effects in far-field become prominent over the coupling effects in near field as the antenna length becomes much smaller in comparison to the resonant wavelength of interacting light at M2 [28]. The optical trapping of electric and magnetic fields within the dielectric spacer for thicker films is shown in Fig. 8. The strong confinement of these EM fields leads to enhanced absorption in our MM.

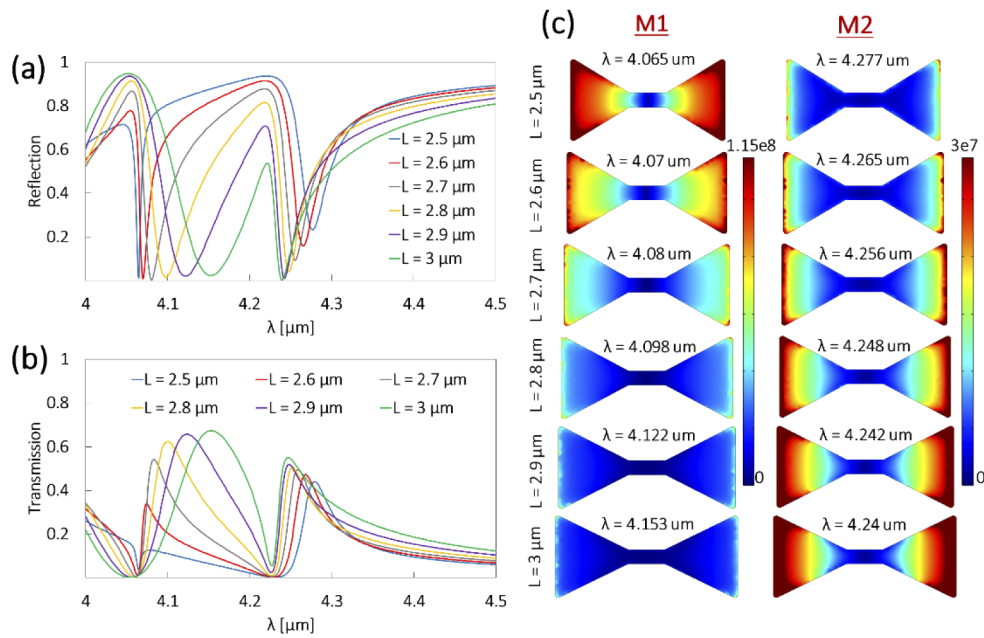


Fig. 7. FEM simulation results (a) R and (b) T spectra for variation of L (c) Surface E-field distribution at S1 for plasmonic state in first band M1 and plasmonic state in second band M2 at the LSP wavelengths corresponding to each L varied.

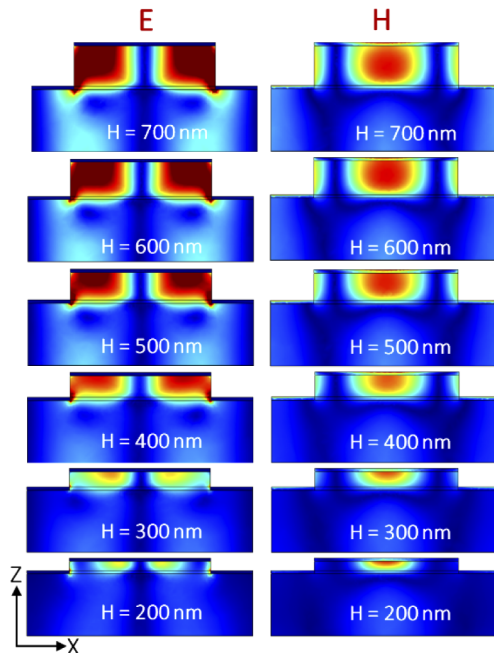


Fig. 8. Effect of varying H of the absorber FEM simulation results showing longitudinal ZX E-field (column 1) and H-field (column 2) distributions as a function of increasing H .

Acknowledgements

AN thanks IIT Delhi and acknowledges Overseas Visiting Doctoral Fellowship from the Science and Engineering Research Board (SERB) of India. AD acknowledges the support of the Ministry of Human Resource Development of India (RP03417G) and Dr. P. Liang for the support in computations. XX acknowledges the support of the US National Science Foundation (CBET-1804377).

Disclosures

The authors declare no conflicts of interest.

References

1. V. M. Shalaev, "Optical negative-index metamaterials," *Nat. Photonics* **1**(1), 41–48 (2007).
2. J. B. Pendry, "Negative Refraction Makes a Perfect Lens," *Phys. Rev. Lett.* **85**(18), 3966–3969 (2000).
3. N. I. Landy, S. Sajuyigbe, J. J. Mock, D. R. Smith, and W. J. Padilla, "Perfect metamaterial absorber," *Phys. Rev. Lett.* **100**(20), 207402 (2008).
4. X. Liu, T. Tyler, T. Starr, A. F. Starr, N. M. Jokerst, and W. J. Padilla, "Taming the blackbody with infrared metamaterials as selective thermal emitters," *Phys. Rev. Lett.* **107**(4), 045901 (2011).
5. R. Li, D. Wu, Y. Liu, L. Yu, Z. Yu, and H. Ye, "Infrared plasmonic refractive index sensor with ultra-high figure of merit based on the optimized all-metal grating," *Nanoscale Res. Lett.* **12**(1), 1 (2017).
6. D. Wu, Y. Liu, R. Li, L. Chen, R. Ma, C. Liu, and H. Ye, "Infrared perfect ultra-narrow band absorber as plasmonic sensor," *Nanoscale Res. Lett.* **11**(1), 1 (2016).
7. A. Moreau, C. Ciraci, J. J. Mock, D. R. Smith, R. T. Hill, A. Chilkoti, Q. Wang, and B. J. Wiley, "Controlled-Reflectance Surfaces with Film-Coupled Colloidal Nanoantennas," *Nature* **492**(7427), 86–89 (2012).
8. M. J. Rozin, D. A. Rosen, T. J. Dill, and A. R. Tao, "Colloidal Metasurfaces Displaying near-Ideal and Tunable Light Absorbance in the Infrared," *Nat. Commun.* **6**(1), 7325 (2015).
9. N. Liu, M. Mesch, T. Weiss, M. Hentschel, and H. Giessen, "Infrared Perfect Absorber and Its Application as Plasmonic Sensor," *Nano Lett.* **10**(7), 2342–2348 (2010).
10. M. Wu, X. Zhao, J. Zhang, J. Schalch, G. Duan, K. Cremin, R. D. Averitt, and X. Zhang, "A three-dimensional all-metal terahertz metamaterial perfect absorber," *Appl. Phys. Lett.* **111**(5), 051101 (2017).
11. Y. Cui, Y. He, Y. Jin, F. Ding, L. Yang, Y. Ye, S. Zhong, Y. Lin, and S. He, "Plasmonic and metamaterial structures as electromagnetic absorbers," *Laser Photonics Rev.* **8**(4), 495–520 (2014).
12. Z. Yong, S. Zhang, C. Gong, and S. He, "Narrow band perfect absorber for maximum localized magnetic and electric field enhancement and sensing applications," *Sci. Rep.* **6**(1), 24063 (2016).
13. X. Ao, X. Wang, G. Yin, K. Dang, Y. Xue, and S. He, "Broadband Metallic Absorber on a Non-Planar Substrate," *Small* **11**(13), 1526–1530 (2015).
14. B. J. Lee, L. P. Wang, and Z. M. Zhang, "Coherent Thermal Emission by Excitation of Magnetic Polaritons Between Periodic Strips and a Metallic Film," *Opt. Express* **16**(15), 11328 (2008).
15. K. Aydin, V. E. Ferry, R. M. Briggs, and H. A. Atwater, "Broadband Polarization-Independent Resonant Light Absorption Using Ultrathin Plasmonic Super Absorbers," *Nat. Commun.* **2**(1), 517 (2011).
16. N. Zhou, E. C. Kinzel, and X. Xu, "Nanoscale ridge aperture as near-field transducer for heat-assisted magnetic recording," *Appl. Opt.* **50**(31), G42 (2011).
17. S. Kang, Z. Qian, V. Rajaram, S. D. Calisgan, A. Alù, and M. Rinaldi, "Ultra-Narrowband Metamaterial Absorbers for High Spectral Resolution Infrared Spectroscopy," *Adv. Opt. Mater.* **7**(2), 1801236 (2019).
18. Y. Huang, J. Luo, M. Pu, Y. Guo, Z. Zhao, X. Ma, X. Li, and X. Luo, "Catenary electromagnetics for ultra-broadband lightweight absorbers and large-scale flat antennas," *Adv. Sci.* **6**(7), 1801691 (2019).
19. J. Tong, F. Suo, J. Ma, L. Y. Tobing, L. Qian, and D. H. Zhang, "Surface plasmon enhanced infrared photodetection," *Opto-Electron. Adv.* **3**(1), 18002601–18002610 (2019).
20. C. Wu, B. Neuner III, G. Shvets, J. John, A. Milder, B. Zollars, and S. Savoy, "Large-area wide-angle spectrally selective plasmonic absorber," *Phys. Rev. B* **84**(7), 075102 (2011).
21. T. Grosjean, M. Mivelle, F. I. Baida, G. W. Burr, and U. C. Fischer, "Diabolo nanoantenna for enhancing and confining the magnetic optical field," *Nano Lett.* **11**(3), 1009–1013 (2011).
22. Y. Chen, J. Chu, and X. Xu, "Plasmonic multibowtie aperture antenna with Fano resonance for nanoscale spectral sorting," *ACS Photonics* **3**(9), 1689–1697 (2016).
23. N. Zhou, E. C. Kinzel, and X. Xu, "Complementary bowtie aperture for localizing and enhancing optical magnetic field," *Opt. Lett.* **36**(15), 2764 (2011).
24. M. Farsari and B. N. Chichkov, "Two-photon fabrication," *Nat. Photonics* **3**(8), 450–452 (2009).
25. COMSOL Multiphysics® v. 5.3. www.comsol.com. COMSOL AB. Stockholm, Sweden.
26. R. L. Olmon, B. Slovick, T. W. Johnson, D. Shelton, S. H. Oh, G. D. Boreman, and M. B. Raschke, "Optical dielectric function of gold," *Phys. Rev. B* **86**(23), 235147 (2012).

27. V. Krápek, A. Konečná, M. Horák, F. Ligmajer, M. Stöger-Pollach, M. Hrtoň, J. Babocký, and T. Šikola, “Independent engineering of individual plasmon modes in plasmonic dimers with conductive and capacitive coupling,” *Nanophotonics* **9**(3), 623–632 (2019).
28. B. Lamprecht, G. Schider, R. T. Lechner, H. Ditlbacher, J. R. Krenn, A. Leitner, and F. R. Aussenegg, “Metal nanoparticle gratings: influence of dipolar particle interaction on the plasmon resonance,” *Phys. Rev. Lett.* **84**(20), 4721–4724 (2000).
29. H. T. Chen, “Interference theory of metamaterial perfect absorbers,” *Opt. Express* **20**(7), 7165 (2012).
30. L. Huang, D. R. Chowdhury, S. Ramani, M. T. Reiten, S. N. Luo, A. K. Azad, A. J. Taylor, and H. T. Chen, “Impact of resonator geometry and its coupling with ground plane on ultrathin metamaterial perfect absorbers,” *Appl. Phys. Lett.* **101**(10), 101102 (2012).
31. L. Huang, D. R. Chowdhury, S. Ramani, M. T. Reiten, S. N. Luo, A. J. Taylor, and H. T. Chen, “Experimental demonstration of terahertz metamaterial absorbers with a broad and flat high absorption band,” *Opt. Lett.* **37**(2), 154 (2012).
32. G. Duan, J. Schalch, X. Zhao, J. Zhang, R. D. Averitt, and X. Zhang, “Analysis of the thickness dependence of metamaterial absorbers at terahertz frequencies,” *Opt. Express* **26**(3), 2242 (2018).
33. W. L. Barnes, A. Dereux, and T. W. Ebbesen, “Surface plasmon subwavelength optics,” *Nature* **424**(6950), 824–830 (2003).
34. N. Gupta and A. Dhawan, “Bridged-bowtie and cross bridged-bowtie nanohole arrays as SERS substrates with hotspot tunability and multi-wavelength SERS response,” *Opt. Express* **26**(14), 17899 (2018).
35. B. Gallinet and O. J. F. Martin, “Relation between Near-Field and Far-Field Properties of Plasmonic Fano Resonances,” *Opt. Express* **19**(22), 22167 (2011).
36. B. Gallinet and O. J. F. Martin, “Influence of electromagnetic interactions on the line shape of plasmonic Fano resonances,” *ACS Nano* **5**(11), 8999–9008 (2011).
37. C. Wu, A. B. Khanikaev, R. Adato, N. Arju, A. A. Yanik, H. Altug, and G. Shvets, “Fano-resonant asymmetric metamaterials for ultrasensitive spectroscopy and identification of molecular monolayers,” *Nat. Mater.* **11**(1), 69–75 (2012).
38. A. B. Khanikaev, C. Wu, and G. Shvets, “Fano-resonant metamaterials and their applications,” *Nanophotonics* **2**(4), 247–264 (2013).